Microscopic origin of resistance drift in the amorphous state of the phase-change compound GeTe

S. Gabardi,[1] S. Caravati,[1] G. C. Sosso,[2] J. Behler,[3] and M. Bernasconi[1,*]

[1]*Dipartimento di Scienza dei Materiali, Università di Milano-Bicocca, Via R. Cozzi 55, I-20125, Milano, Italy*
[2]*Department of Chemistry and Applied Biosciences, ETH Zurich, USI Campus, Via Giuseppe Buffi 13, 6900 Lugano, Switzerland*
[3]*Lehrstuhl für Theoretische Chemie, Ruhr-Universität Bochum, D-44780 Bochum, Germany*

Aging is a common feature of the glassy state. In the case of phase-change chalcogenide alloys the aging of the amorphous state is responsible for an increase of the electrical resistance with time. This phenomenon called drift is detrimental in the application of these materials in phase-change nonvolatile memories, which are emerging as promising candidates for storage class memories. By means of combined molecular dynamics and electronic structure calculations based on density functional theory, we have unraveled the atomistic origin of the resistance drift in the prototypical phase-change compound GeTe. The drift results from a widening of the band gap and a reduction of Urbach tails due to structural relaxations leading to the removal of chains of Ge-Ge homopolar bonds. The same structural features are actually responsible for the high mobility above the glass transition which boosts the crystallization speed exploited in the device.

I. INTRODUCTION

Chalcogenide phase-change alloys are widely used in optical storage (digital versatile disk, DVD) and, more recently, also in electronic nonvolatile memories named phase-change memories (PCM). Both applications rest on the fast and reversible phase change between the crystalline and amorphous phases induced by heating either via laser irradiation (DVD) or via Joule effect (PCM) [1]. The two states of the memory can be discriminated thanks to a large difference in optical reflectivity (in DVD) and electrical resistivity (in PCM) between the two phases. The $Ge_2Sb_2Te_5$ (GST) compound is presently the material of choice for PCM applications because it provides a good compromise between transformation speed and stability of the amorphous phase [2–4]. However, also the binary GeTe compound with various doping [5] and other tellurides alloys [6,7] are under scrutiny for the higher stability of their amorphous phase which is of interest for applications at high temperatures, e.g., in automotive electronics.

In PCM the readout of the logical state consists of a measurement of resistance at low bias, while writing/erasing operations require higher voltage pulses to induce either the melting of the crystal and subsequent amorphization or the recrystallization of the amorphous phase. While the crystal is stable, the metastable amorphous phase is subject to aging which leads to an increase in the electrical resistivity with time. This phenomenon called drift [2] is described by a power law function $R = R_o(t/t_o)^\nu$, where R and R_o are the resistance at time t and t_o and ν is the drift exponent. The drift should be kept as low as possible as it affects the reliability of PCM and it hinders the realization of multilevel cells [8]. It would then be desirable to achieve a full microscopic understanding of this process to keep it under control and eventually to minimize its effects by a suitable tuning of the alloy composition [9] without sacrificing the other functional characteristics.

Since in PCM the amorphous phase is under compressive stress due to the embedding in the denser crystalline matrix, it

was proposed that the drift arises from stress relief upon time leading to an increase in the band gap [10,11]. This scenario seemed to be confirmed by the measurement of a lower drift in eventually stress-free GST nanowires [12]. However, since later measurements of both PCM and stress-free, as-deposited amorphous GST films gave the same drift exponent [13], an alternative scenario seemed more viable in which the drift was actually resulting from relaxations of local defective structures of the amorphous phase toward a more stable configuration [14]. This aging process would not lead to a more crystallinelike material, but to a less defective, more ideal glass. In fact, the crystal actually displays a lower resistivity than the amorphous phase while the drift leads to an increase of resistance over time.

Optical ellipsometry measurements of GST upon drift have indeed shown a widening of the band gap and a reduction of Urbach tails somehow related to structural defects [15]. Extended Urbach tails and a large density of deep defect states in the gap have actually been detected in amorphous GeTe (a-GeTe) by modulated photocurrent experiments [16]. Widening of the band gap and reduction of Urbach tails both concur to increase the resistivity of the amorphous phase as both these effects lead to an increase of the activation energy for carrier generation. In fact, the conductivity of the amorphous phase is believed to be due to carriers injected via thermal excitations from states inside the mobility gap. This process is further assisted by the electric field according to the Poole-Frenkel mechanism [17]. The role of deep defect states in the conduction mechanism and then in the drift phenomenon is instead more controversial [18].

The atomistic origin of the localized states in the Urbach tails or deep in the gap is, however, unknown. The first result linking structural features of the amorphous phase with the resistance drift came recently from Ge K-edge x-ray absorption near-edge structure (XANES) spectra of GST [19]. In the amorphous phase of GST as well as of GeTe, most atoms are in pyramidal or defective octahedral configurations but for a minority fraction of Ge atoms which display a tetrahedral bonding geometry [20–23]. It was shown that the drift is correlated with the reduction of a steplike feature in the

*marco.bernasconi@mater.unimib.it

pre-edge XANES spectra [19] that was previously assigned to tetrahedrally coordinated Ge atoms [25]. The results seem thus to suggest that the drift is correlated with a reduction of Ge in tetrahedral sites. How the conversion of tetrahedral sites into defective octahedral/pyramidal sites would affect the electronic states of the amorphous is still an open issue which has to be addressed by electronic structure calculations.

In this paper, we move this crucial step further by providing a link between electronic states and the specific structural features whose relaxation leads to the resistance drift.

To this end, we computed the electronic structure at the level of density functional theory (DFT) of large, 1728-atom models of a-GeTe. The models were generated by quenching from the melt within molecular dynamics (MD) simulations employing an interatomic potential [26] generated by fitting a large database of DFT energies with a neural network (NN) method [27]. The aging process was accelerated either by annealing at 500 K or by using the metadynamics technique [28–30]. The simulations revealed that the widening of the band gap is due to the removal of chains of homopolar Ge-Ge bonds.

II. COMPUTATIONAL DETAILS

We performed molecular dynamics (MD) simulations by employing an interatomic potential [26] generated by fitting a large database of DFT energies with a neural network (NN) method [27]. The database consists of the total energies of about 30 000 configurations of 64-, 96-, and 216-atom supercells computed with the Perdew-Burke-Ernzerhof (PBE) exchange and correlation functional [31] and norm conserving pseudopotentials. The transferability of the NN potential was formerly validated by simulations of the liquid, amorphous, and crystalline phases [26,32–35]. The simulations were performed with the NN code RuNNer [36] with a cubic supercell by using the DL_POLY code as MD driver [37]. The time step was set to 2 fs and temperature was enforced by a stochastic thermostat [38].

We generated two 1728-atom amorphous models by quenching from the melt at fixed density from 1000 K to 300 K in 100 ps. In one model (model 1) the density was equal to the theoretical equilibrium density of 0.0335 atoms/$\mathring{A}^3$. In the second model (model 2), a higher density of 0.0357 atoms/$\mathring{A}^3$ was chosen aiming at generating a larger concentration of defect states in the gap according to the suggestion of Ref. [39]. This second model was then scaled and further optimized at the density of model 1.

The resulting models were then optimized at the DFT-PBE level by solving the Kohn-Sham (KS) equation with the Quickstep scheme as implemented in the CP2k suite of programs [40]. In this approach the KS orbitals are expanded in Gaussian type orbitals (GTOs) and the charge density is represented with an auxiliary plane waves basis with a cutoff of 100 Ry to efficiently solve the Poisson equation. Gaussian-type pseudopotentials [41] with four and six valence electrons were adopted for Ge and Te. The KS orbitals were expanded in a triple-ζ-valence plus polarization (TZVP) GTOs basis set. Brillouin zone integration was restricted to the supercell Γ point.

The structure of the amorphous models was analyzed by computing the total and partial pair correlation functions from the atomic positions optimized at the DFT-PBE level and from harmonic phonons computed with the NN potential as described below. Since the NN potential reproduces well the phonon density of states of a-GeTe [33], we did not compute phonons by DFT in our large (1728 atoms) cell.

The partial pair correlation functions are defined by

$$g_{\alpha\beta}(r) = \frac{1}{N_\alpha \rho_\beta} \sum_{I \in \alpha, J \in \beta} \langle \delta(\mathbf{r} + \mathbf{R}_I - \mathbf{R}_J) \rangle, \quad (1)$$

where N_α is the number of atoms of species α and ρ_β the density of atoms of species β. The total pair correlation function is given in turn by

$$g(r) = \sum_{\alpha\beta} x_\alpha x_\beta g_{\alpha\beta}(r), \quad (2)$$

where x_α is the number concentration of species α [42]. The thermal average $\langle \cdots \rangle$ is restricted to the the harmonic approximation by replacing the δ function in Eq. (1) with a Gaussian function of variance σ [43]

$$\sigma^2 = \langle [\mathbf{d} \cdot (\mathbf{u}_I - \mathbf{u}_J)]^2 \rangle, \quad (3)$$

where $\mathbf{u}_I$ is the displacement of the Ith atom with respect to the equilibrium position $\mathbf{R}_I$, and $\mathbf{d}$ is a unitary vector along the direction of $\mathbf{R}_I - \mathbf{R}_J$. The thermal average $\langle \cdots \rangle$ is then computed from harmonic phonons as

$$\langle \mathbf{u}_I \mathbf{u}_J \rangle = \sum_n \frac{\hbar}{\omega_n} \frac{\mathbf{e}(n,I)}{\sqrt{M_I}} \frac{\mathbf{e}(n,J)}{\sqrt{M_J}} \left[n_B(\omega_n) + \frac{1}{2} \right], \quad (4)$$

where M_I is the mass of Ith atom, and ω_n and $\mathbf{e}(n,I)$ are frequencies and eigenvectors of the nth harmonic phonon. The temperature dependence is introduced by the Bose factor $n_B(\omega_n) + \frac{1}{2}$ whose classical limit is $k_B T/(\hbar\omega_n)$.

In order to study the Urbach tails and the defect states in the gap, the KS energies have been computed with the exchange-correlation potential proposed by Engel and Vosko (EV) [44] and with the self-consistent electronic density at the PBE level. This functional is known to better reproduce the band gap and it is less computationally demanding than the hybrid functionals used previously with small models [45]. We verified that the individual KS states are very similar in PBE and EV calculations, but for the fact that the larger gap in EV enhances the localization of defect states in the gap and at the band edges. To quantify the localization properties of individual KS states, we have computed the inverse participation ratio (IPR), which is defined for the ith KS state by $\sum_j c_{ij}^4/(\sum_j c_{ij}^2)^2$ where j runs over the GTOs of the basis set and c_{ij} are the expansion coefficients of the ith KS state in GTOs. The larger the IPR the more localized is the corresponding KS state. The electronic density of states (DOS) was computed from KS orbitals at Γ point broadened with a Gaussian function with variance of 27 meV.

To quantify the widening of the band gap, we computed the optical Tauc gap that is defined as the energy E for which the linear extrapolation of the function $E\sqrt{\varepsilon_2(E)}$ becomes zero, where $\varepsilon_2(E)$ is the imaginary part of the dielectric function. To this end, we computed $\varepsilon_2(E)$ in the random phase

approximation (RPA) from KS orbitals with the EV functional as

$$\varepsilon_2(\hbar\omega) = \frac{8\pi^2}{3V_o\omega^2}\sum_{v,c}|\langle c|\mathbf{p}|v\rangle|^2\delta(\hbar\omega - E_c + E_v), \quad (5)$$

where E_c and E_v are the energies of conduction and valence states and V_o is the unit cell volume. In the actual calculation the δ functions are substituted by a Gaussian function with variance of 0.136 eV. Neglecting local field effects has been proven to be adequate in previous calculations on GeTe [46]. Many body effects in the GW approximation and from the solution of the Bethe-Salpeter equation have also been shown to give negligible contributions [46]. The same approach but for the use of an hybrid functional was employed in our previous study of the optical properties of a-GeTe, a-GST, and a-Sb$_2$Te$_3$ [47].

The aging process was mimicked either by annealing or by the metadynamics technique. The metadynamics method [28–30] is based on a coarse-grained, non-Markovian dynamics in the manifold spanned by few reaction coordinates (collective variables), biased by a history-dependent potential, which drives the system towards the lowest saddle point. The main assumption is that the reaction path could be described on the manifold of few collective coordinates $S_\alpha(\{\mathbf{R}_I\})$, function of the ionic coordinates $\mathbf{R}_I$. In metadynamics simulations the Lagrangian is supplemented by a history-dependent external potential $V(t, S_\alpha(\{\mathbf{R}_I\}))$ which acts on the ionic coordinates. The history-dependent potential is constructed by the accumulation of Gaussian functions, centered at the positions of the $\{S_\alpha\}$ already visited along the trajectory. The potential discourages the system from remaining in the region already visited and pushes it over the lowest energy barrier towards a new local minimum. This method has been applied to study several chemical reactions and structural transformation at surfaces, in the gas phase and in the bulk [29,30]. In our case, we chose two collective variables defined by the partial coordination numbers Ge-Ge and Ge-Te for atoms in Ge-Ge chains. The isotropic Gaussian functions of height 0.124 eV and width of 50 meV were added every 100 MD steps.

III. RESULTS

A. Structural properties of amorphous GeTe

Before discussing the effects of aging on the structural and electronic properties of a-GeTe we here briefly summarize the outcome of previous DFT simulations on the structural properties of amorphous GeTe [21–23]. The models generated by NN simulations reproduce the DFT results [26]. For the sake of comparison we also discuss the structure of Ge$_2$Sb$_2$Te$_5$ (GST) and Sb$_2$Te$_3$ compounds that share many properties with GeTe as reported in Refs. [20–22,45,48–50]. In these compounds we observe a majority of Ge-Te and Sb-Te bonds, although a sizable fraction of Ge-Ge, Ge-Sb, and Sb-Sb bonds, not present in the crystal and thus named wrong bonds, is also found in the amorphous phase. These wrong bonds form chains as it will discussed later on. Te-Te bonds are rare and only form dimers. In all these amorphous compounds, Ge and Sb atoms are mostly fourfold coordinated in the defective-octahedral configuration shown in Fig. 1(a) with bonding angles of 90°
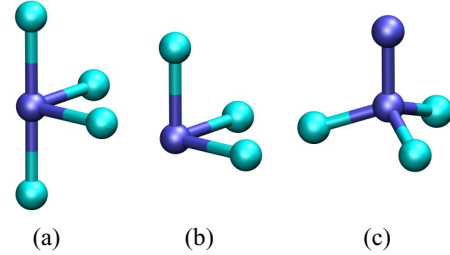

FIG. 1. (Color online) Snapshot of Ge atoms in (a) defective octahedra, (b) pyramids, and (c) tetrahedra with a wrong Ge-Ge bond.

and 180°. A fraction of Ge and Sb atoms and the majority of Te atoms are threefold coordinated in pyramidal configurations [cf. Fig. 1(b)] that can also be seen as defective octahedra with three bonds and bonding angles at 90° only.

Actually, the distribution of the bond lengths for four- or fivefold coordinated Ge and Sb atoms in defective octahedra shows a bimodal shape with three shorter bonds and one or two longer ones. These structures recall a $3 + n(n = 0 - 2)$ geometry similar to the $3 + 3$ bonding coordination in crystalline trigonal GeTe [51], which is a consequence of the formation of $p\sigma$ bonds, including dative bonds from lone pairs of Te atoms [49]. A fraction of Ge atoms of about 20%–30% is, however, in a tetrahedral-like geometry [cf. Fig. 1(c)].

The tetrahedral configuration is promoted by the presence of wrong Ge-Ge bonds as most of the tetrahedra contain at least one Ge-Ge bond. These features identified from amorphous models generated either by DFT or by NN molecular simulations in previous works are shared by the 1728-atom models generated here. The partial pair correlation functions of model 1 and 2 are reported in Fig. 2. Due to the low Debye temperature of GeTe (199 K) [52], the classical approximation and the full quantum expression are indistinguishable on the scale of the figure. About 72% of Ge atoms form at least one homopolar Ge-Ge bond in both models, the Ge-Ge homopolar bonds being in the fraction of about 14% of the total number of bonds (cf. Table I).

A large fraction of Ge-Ge bonds is arranged in chains containing four or more Ge atoms. The fraction of Ge atoms belonging to these chains is in the range 43%–48% as shown in Table I. The distribution of chains length in the model 2 is

TABLE I. Fraction of Ge-Ge bonds (%) over the total number of bonds and fraction of Ge atoms in Ge-Ge chains with four or more Ge atoms for the two models of a-GeTe (model 1 and model 2) before and after annealing at 500 K and for model 2 also after metadynamics simulations. The data after annealing refer to atoms that do not crystallize. Total DFT energy of the 1728-atom models are given in the last column (eV/atom).

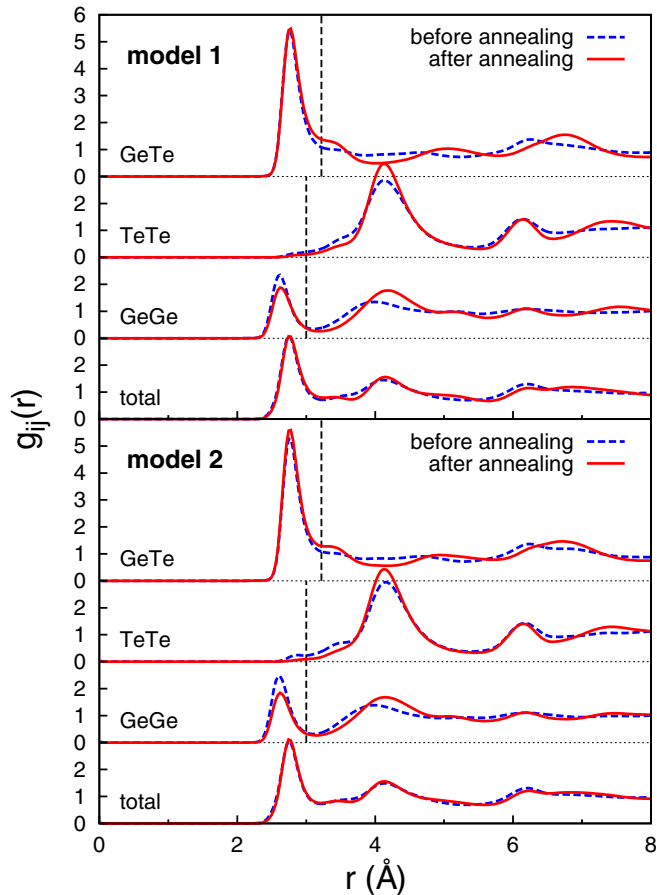|	Ge-Ge bonds (%)	Ge in chains ($\geqslant$4) (%)	Energy (eV/atom)
Model 1	13.9	43.2	0.0
Model 1 annealed	10.2	34.3	−0.019
Model 2	14.5	48.5	−0.001
Model 2 annealed	10.3	31.6	−0.022
Model 2 metadyn.	12.6	39.6	−0.007

FIG. 2. (Color online) Partial pair correlation functions of a-GeTe before and after annealing simulations computed for model 1 and model 2 optimized at the DFT-PBE level with harmonic phonons (see text). Vertical lines are the cutoff used to define the bonds. The shoulder at about 3.2 Å in the annealed models are due to partial crystallization (cf. Ref. [26]).
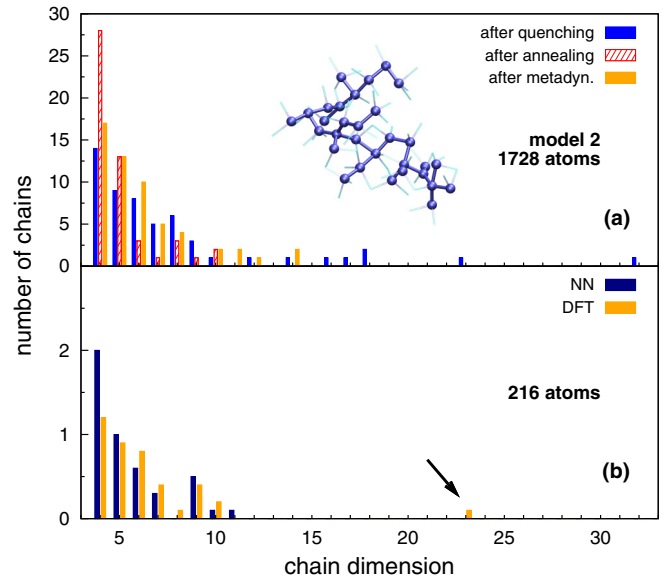

FIG. 3. (Color online) (a) Distribution of the number of Ge-Ge chains as a function of the number of atoms in the chain for the model 2 before, after annealing, and after metadynamics simulations. The Ge atoms are considered bonded when their distance is shorter than 3.0 Å as assigned from the Ge-Ge pair correlation function of the amorphous phase (cf. Fig. 2). Only chains containing at least four Ge atoms are shown including branches and loops. A chain of homopolar bonds is shown in the inset. (b) Distribution of the length (dimension) of chains of homopolar Ge-Ge bonds in ten 216-atom models of a-GeTe generated by quenching from the melt either within NN-MD or DFT-MD as described in Ref. [26]. A long chain in the DFT model is indicated by an arrow. The number of chains is per model, i.e., it is normalized to the number (10) of models.

reported in Fig. 3(a). A similar distribution is found for the other model. The Ge-Ge chains present in the a-GeTe models are not an artifact of the NN potential as they are present also in DFT models of GeTe. The distribution of the chains length and number actually depends on the size of the simulation cell. In order to provide a compelling comparison between NN and DFT results we computed the distribution of chains for ten 216-atom models generated by either DFT or NN simulations. The comparison is reported in Fig. 3(b). The DFT and NN 216-atom models have been used in Ref. [26] to validate the NN potential. We remark that the chains of Ge-Ge bonds are not isolated from the rest of the amorphous network as Ge atoms belonging to the chains are mostly fourfold coordinated and bonded with Te atoms as well.

The percentage of tetrahedra in the models of a-GeTe was quantified by computing the q order parameter introduced in Ref. [53] as a measure of the tetrahedricity of the atomic environments and defined by $q = 1 - \frac{3}{8} \sum_{i>k} (\frac{1}{3} + \cos \theta_{ijk})^2$, where the sum runs over the pairs of atoms bonded to a central atom j and forming a bonding angle θ_{ijk}. The q order parameter can discriminate between different atomic geometries being equal to one for the ideal tetrahedral environment and to zero

for the ideal six-coordinated octahedral environment. In the case of a defective octahedral geometry, $q = 5/8$ for fourfold coordinated atoms and $q = 7/8$ for threefold coordinated atoms in the pyramidal geometry [20]. The distribution of the q order parameter for fourfold coordinated Ge atoms is shown in Fig. 4 for model 2 along with the distribution resolved for Ge atoms which form at least one Ge-Ge bond (homopolar Ge). The coordination number is obtained by integrating the partial pair correlation functions up to the threshold cutoff given in Fig. 2. As shown in Fig. 4, Ge atoms with homopolar bonds have a higher degree of tetrahedricity as the peak of the corresponding q distribution is closer to one. Similar results are found for model 1.

The fraction of atoms in tetrahedral coordination is obtained by integrating the q distribution for fourfold coordinated atoms from 0.8 to 1. This threshold in the q parameter was shown to be a good choice to identify the tetrahedra in the GeTe, GeSbTe, InGeTe$_2$, and InSbTe amorphous alloys [23,54–56]. The fraction of Ge atoms in tetrahedral configurations in models 1 and 2 are 29% and 32% of the total number of Ge atoms.

B. Electronic structure of amorphous GeTe

A zooming of the electronic DOS and the IPR close to the band gap are reported in Fig. 5(b) for the two models.
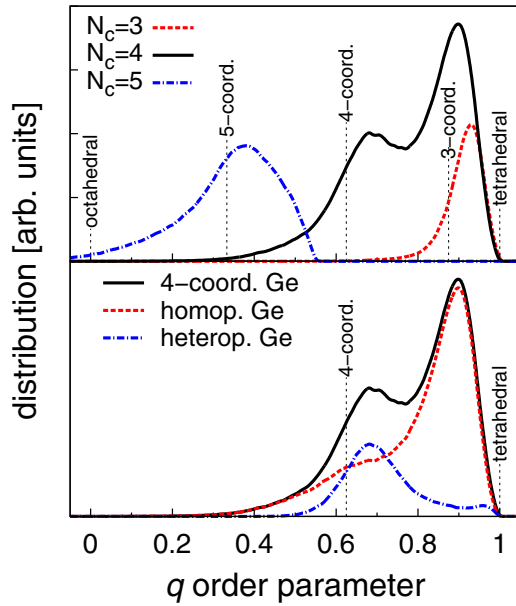
FIG. 4. (Color online) Distribution of the local order parameter q for tetrahedricity (see text) for Ge atoms with different coordination (N_c) in model 2 of a-GeTe. Vertical lines indicate the values of q for selected ideal geometries. The distribution is further resolved for fourfold coordinated Ge atoms with or without homopolar bonds in the lower panel.

The DOS in the full energy range is given in Fig. 6. A broad distribution of defect states is found around a pseudogap in the DOS with localization (IPR) decreasing toward the band edges. The number of deep states is larger in the model generated at higher density (model 2).

Among the several attempts we made to find a correlation between the localized states and possible structural features, a clear correlation was found with the short chains of Ge-Ge homopolar bonds, described in the previous section. The DOS projected on atoms belonging to Ge-Ge chains of different length is reported in Fig. 5(a) and a snapshot of the KS states, mostly localized on Ge-Ge chains, is shown in Fig. S3 of the Supplemental Material (SM) [24]. As we will see in the next section, the partial removal of these chains of Ge-Ge bonds leads to a reduction of defect states in the gap and to an overall widening of the band gap.

C. Simulation of aging of amorphous GeTe

To accelerate the structural relaxations that are supposed to lead to the drift in the electrical resistance, we annealed the two models at 500 K for 1.5 ns in NN-MD simulations and we then optimized the geometry of the resulting model at the DFT-PBE level. The DOS and IPR of the annealed models are compared with those of the pristine ones close to the band gap in Figs. 5(c) and 5(d). The corresponding DOS over the full energy range are shown in Fig. 6.

The annealing clearly induces a decrease in the number of the states in the gap, an increase of their localization, and an overall widening of the gap due to the reduction of Urbach tails. This can be traced back to an overall decrease in the fraction of atoms belonging to the Ge-Ge chains and in a

reduction of the average length of the chains as shown in Fig. 3. This transformation, however, requires a more careful analysis because the annealing of a-GeTe at 500 K also induced the formation of small crystallites, similar to what we observed in the previous simulations of the homogeneous crystallization [34]. In the two models after annealing, an overall fraction of crystalline atoms of about 10%–13% was found by using the local order parameter Q_6 introduced in Refs. [57,58] and already applied in our previous simulations to which we refer to for all the computational details [34]. Still, we observed a reduction in the fraction of atoms belonging to longer chains (with at least four Ge atoms) also by considering the subset of atoms that do not crystallize as shown in Table I. The reduction in the fraction of Ge-Ge bonds is also clear from the partial pair correlation functions before and after the annealing reported in Fig. 2.

In order to obtain an independent, compelling demonstration that the removal of Ge-Ge chains leads to a widening of the band gap, we performed NN metadynamics simulations. This technique allows breaking the Ge-Ge bonds in an affordable simulation time even at lower temperatures where crystal nucleation does not occur. As briefly described in Sec. II, the method [28–30] is based on a coarse-grained, non-Markovian dynamics in the manifold spanned by few reaction coordinates (collective variables), biased by a history-dependent potential, which drives the system towards the lowest saddle point.

In our case, we chose two collective variables defined by the partial coordination numbers Ge-Ge and Ge-Te for atoms in Ge-Ge chains. We performed a chain of subsequent simulations by changing the subset of atoms included in the definition of the collective variables in order to progressively remove different Ge-Ge chains. After a well-tempered [29,30] metadynamics simulation 4 ns long, the geometry of the resulting model was optimized at the DFT-PBE level. The final configuration of model 2 was about 10.8 eV (1728-atom) lower in energy than the initial one optimized at DFT-PBE level before the metadynamics was applied (cf. Table I). In the final state after metadynamics, a sizable fraction of long Ge-Ge chains was indeed removed as shown in Table I and Fig. 3 and no crystallites were formed. The reduction in the fraction of Ge-Ge bonds is also clear from the partial pair correlation functions before and after metadynamics reported in Fig. S4 in SM [24].

A zooming of the DOS and IPR close to the band gap before and after metadynamics simulations are compared in Fig. 7. The DOS over the full spectral range are compared in Fig. 6. The decrease in the number of Ge-Ge chains obtained from metadynamics clearly reduces the states in the gap and enhances their localization (IPR). The remaining states in the gap are still localized mostly on Ge-Ge chains.

The removal of Ge-Ge chains thus leads to a reduction of Urbach tails but also to a widening of the band gap that we have quantified by computing the Tauc optical gap from the imaginary part of the dielectric function as described in Sec. II. The Tauc plots for the model before and after the metadynamics simulations are shown in Fig. 8. After metadynamics simulations the Tauc optical gap increases by about 20 meV that is even quantitatively close to the increase of the Tauc gap by 40 meV measured experimentally in GST upon drift [15].
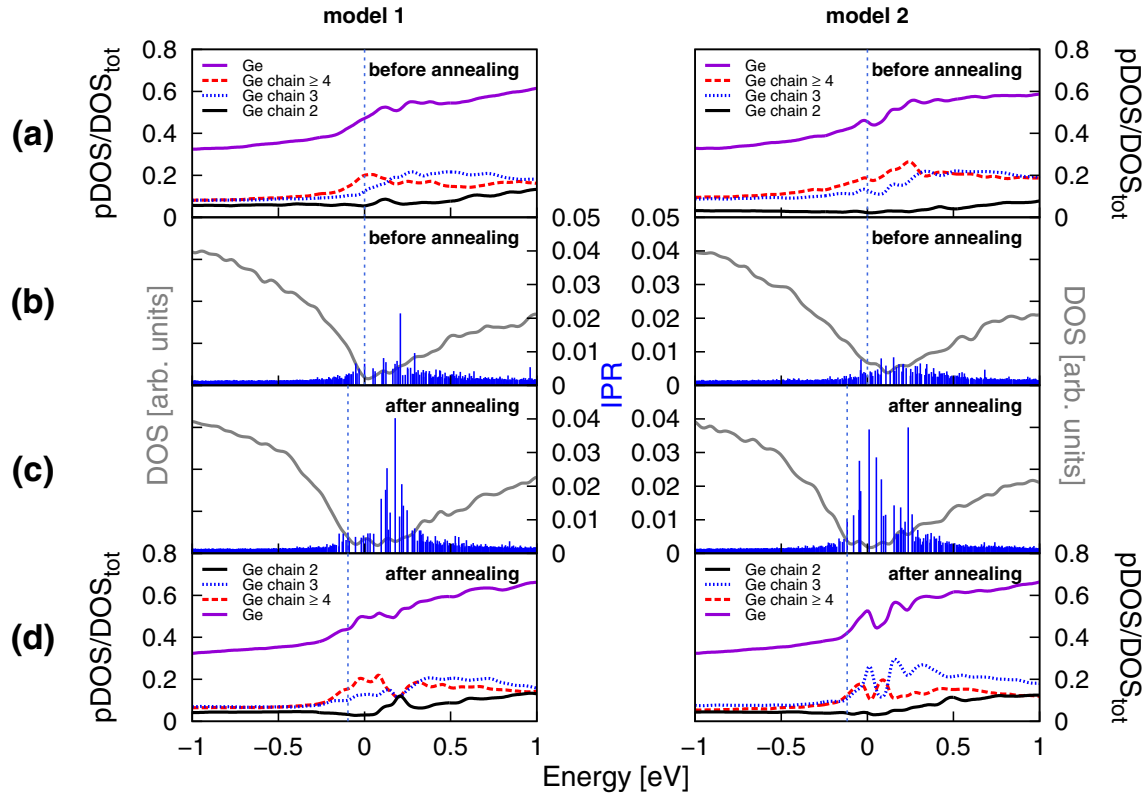
FIG. 5. (Color online) (a) Projection of the electronic DOS on Ge atoms belonging to Ge chains of different lengths normalized to the total DOS (model 1 and model 2 in the left and right panels). (b) The total DOS and the inverse participation ratio (IPR; see text) for the two models of a-GeTe before annealing. Panels (c) and (d) are the equivalent of panels (b) and (a) after annealing at 500 K (see text). The Engel-Vosko functional was used, the corresponding plots for the PBE functional are given in Fig. S1 in the Supplemental Material (SM) [24]. The DOS before and after annealing are aligned at the lowest energy states at about -14 eV as shown in Fig. 6. The vertical dashed line indicates the highest occupied KS state, which coincides with the zero of energy before annealing.

As we already mentioned in Sec. III A, homopolar Ge-Ge bonds are known to favor a tetrahedral coordination of Ge.
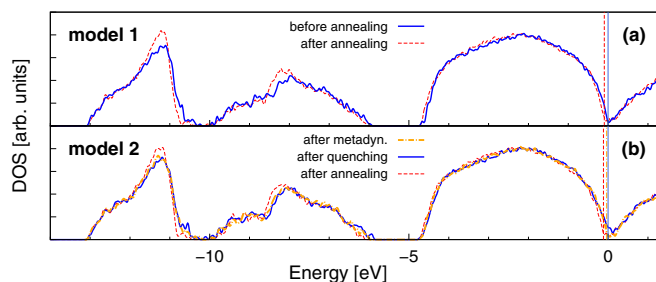

FIG. 6. (Color online) Electronic density of states (DOS) of (a) model 1 and (b) model 2 before (continuous line) and after (dashed line) annealing in the full energy range. For model 2 the DOS is shown also after metadynamics simulations (dot-dashed line). The Engel-Vosko functional was used; the corresponding plots for the PBE functionals are given in Fig. S2 in the SM [24]. The DOS before and after annealing/metadynamics are aligned at the lowest energy states at about -14 eV, which also leads to an alignment of the lower edges of the p-like bands at about -4.5 eV. The vertical dashed line indicates the highest occupied Kohn-Sham (KS) state which coincides with the zero of energy before annealing. The DOS was computed from KS orbitals at the supercell Γ-point broadened with a Gaussian function with variance of 27 meV.

This feature was found in earlier simulations of GST and GeTe [20,23] and it was better clarified on the basis of the analysis of bond energies in a more recent work [59]. We should thus expect that the decrease in the fraction of Ge-Ge bonds due to the removal of Ge-Ge chains would also lead to a reduction of tetrahedra which are favored by homopolar bonds, in agreement with the XANES measurements of Ref. [19]. We remark that the area of the XANES spectral feature associated with tetrahedra decreases by at most 10% upon drift [19]. Since only about 30% of Ge atoms are in tetrahedral geometry (cf. Sec. III A), the change in the XANES signal involves about 3% of Ge atoms. After metadynamics simulations the fraction of tetrahedral Ge in model 2 decreases from 32% to 30% of the total number of Ge atoms which is a reduction even quantitatively consistent with the XANES data. We remark that the fraction of Ge atoms with at least one wrong bond in model 2 is instead 72% or 66% of the total number of Ge atoms, before or after metadynamics simulations. The reduction of tetrahedra can thus be seen as a side effect of the removal of a larger fraction of chained Ge-Ge wrong bonds upon drift. Note that a correlation between a lower fraction of homopolar Ge-Ge bonds and a larger band gap was also proposed previously on the basis of a statistical analysis of the DFT electronic structure of several small models of a-GeTe [60].

We remark that similar chains of wrong bonds (Ge-Ge, Ge-Sb, and Sb-Sb) are present also in 459-atom DFT models
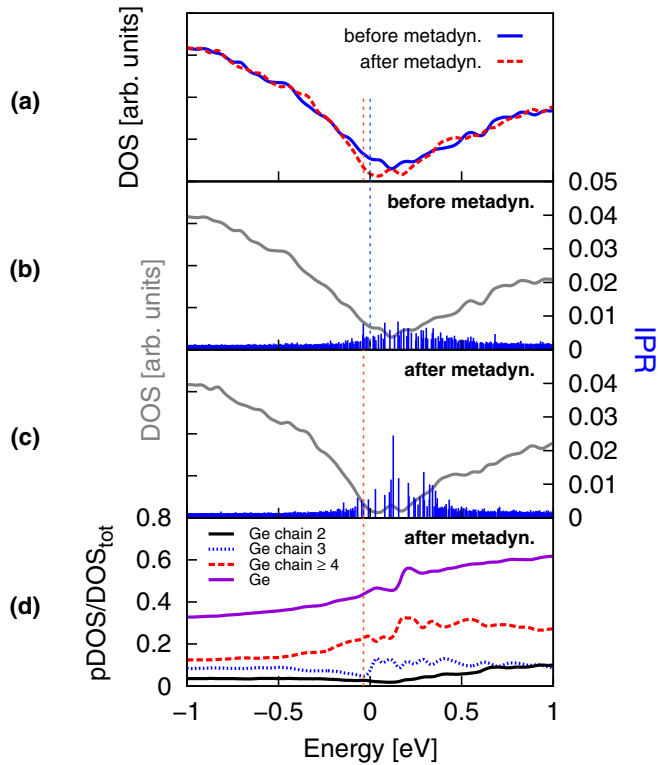
FIG. 7. (Color online) (a) Electronic DOS close to the band gap of model 2 of a-GeTe before (continuous line) and after (dashed line) metadynamics simulations (cf. Fig. 5). (b) Inverse participation ratio (IPR) superimposed to the DOS before and (c) after metadynamics simulations. (d) Projection of the DOS on Ge atoms belonging to Ge chains of different lengths normalized to the total DOS for the model after metadynamics simulations; the corresponding plot before metadynamics is shown in the right panel of Fig. 5(a). The Engel-Vosko functional was used; the corresponding plots for the PBE functional are given in Fig. S5 in SM [24]. The DOS are aligned as in Fig. 5.

of a-GST as shown in Fig. 9. Chains of Sb-Sb bonds are also found in the DFT model of a-Sb$_2$Te$_3$ of Ref. [50]. Therefore, the outcome of the present simulations demonstrating that the resistance drift in a-GeTe is due to the gap widening originating from the removal of wrong bonds might be well transferred to other GeSbTe phase-change alloys.

IV. DISCUSSION AND CONCLUSIONS

In summary, by means of combined large scale MD simulations and DFT electronic structure calculations we have demonstrated that the drift in the electronic resistance in a-GeTe arises from structural relaxations consisting of the removal of chains of homopolar Ge-Ge bonds. The removal of these wrong bonds, not present in the crystal, leads to a widening of the band gap and to a reduction of Urbach tails that can both concur to increase the electronic resistance. Since Ge-Ge bonds favor tetrahedral coordination of Ge atoms, their partial removal also leads to a reduction of tetrahedra in agreement with experimental XANES spectra. The latter is somehow a side effect of a much larger reduction of Ge-Ge bonds in long (⩾four Ge atoms) chains of homopolar bonds.
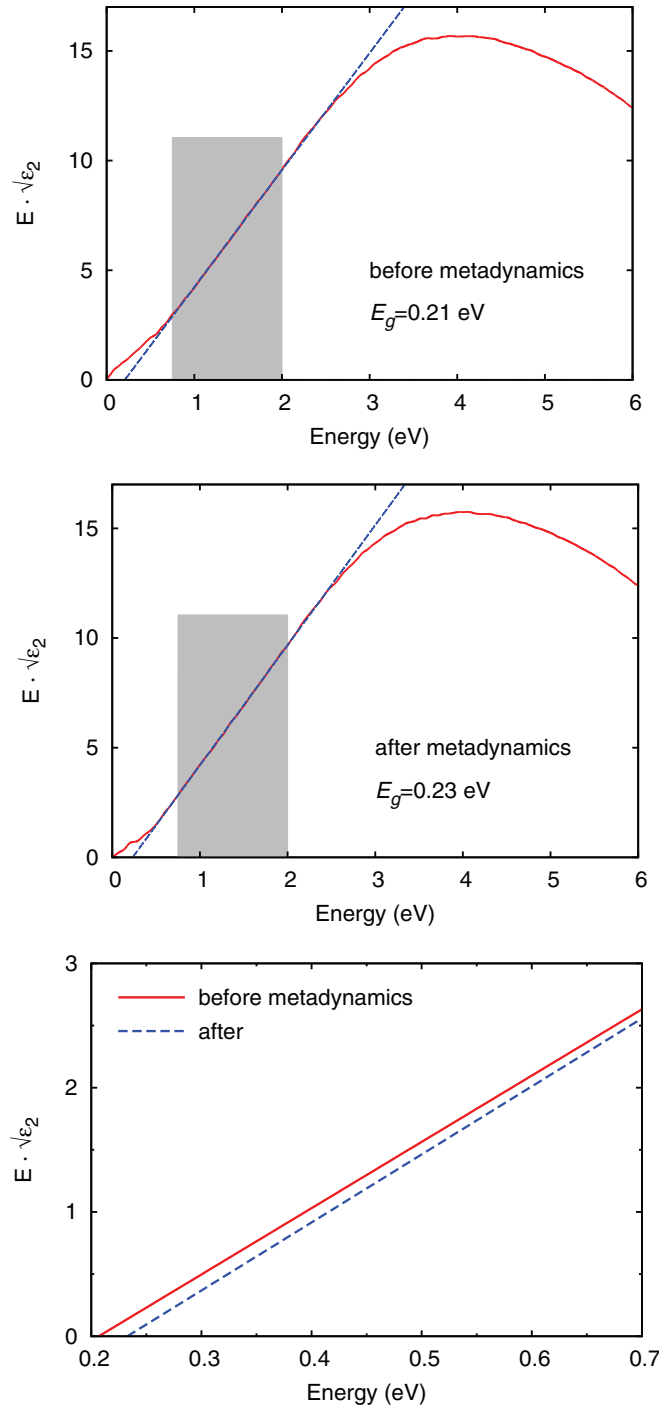

FIG. 8. (Color online) Tauc plot of the a-GeTe model before (top panel) and after (central panel) metadynamics simulations. The shaded area indicate the range of energies used for the linear extrapolation that gives the Tauc optical gap. The bottom panel shows a zoom of the linear plot close to the Tauc gap. The Engel-Vosko functional was used to compute the imaginary part of the dielectric function $\varepsilon_2(E)$.

Similar chains of wrong bonds (Ge-Ge, Ge-Sb, and Sb-Sb) are present in DFT models of amorphous Ge$_2$Sb$_2$Te$_5$ and Sb$_2$Te$_3$ compounds which suggest that the removal of chains of wrong bonds identified here in a-GeTe can be the source of the resistance drift in GeSbTe alloys at large.
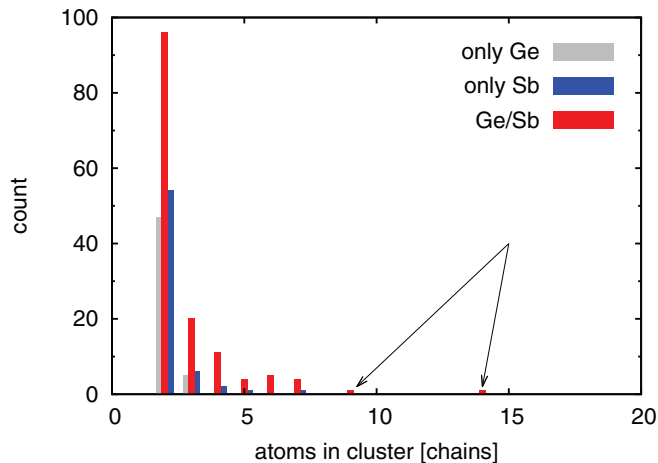
FIG. 9. (Color online) Distribution of the length of chains of wrong bonds in four 459-atom models of amorphous $Ge_2Sb_2Te_5$ generated by quenching from the melt in DFT simulations as described in Ref. [48]. We considered chains formed by Ge-Ge bonds only, Sb-Sb bonds only, or chains containing Ge-Ge, Sb-Sb, and Ge-Sb wrong bonds. Two large chains are indicated by arrows. The atoms in the chains include branches and loops.

It is interesting to note that in GeTe the same structural features (Ge-Ge chains), identified here as the source of the resistance drift in the amorphous phase below the glass transition T_g, have also been shown to be involved in the dynamics of the supercooled liquid above T_g [35]. By means of NN-MD simulations of GeTe, we have previously uncovered the emergence of dynamical heterogeneities in supercooled liquid GeTe, responsible for the breakdown of the Stokes-Einstein relation between viscosity and diffusivity [32,35]. This behavior, typical of fragile liquids [61,62], is responsible for the persistence of a high atomic mobility in the supercooled liquid down to temperatures very close to T_g. Such a feature actually boosts both the nucleation rate and the crystal growth velocity exploited in PCM [63]. In fact, in the set operation of

PCM the amorphous phase is rapidly brought to a temperature much above T_g where it is expected to behave as a supercooled liquid [64]. The NN-MD simulations [35] revealed that fast and slow moving atoms tend to cluster in spatially separated domains giving rise to dynamical heterogeneities with the fast moving atoms actually clustering around chains of homopolar Ge-Ge bonds. The dynamical heterogeneities in supercooled liquid GeTe thus originates from structural heterogeneities in the form of chains of homopolar bonds. The outcomes reported here further demonstrate at the atomistic level a connection between the fragility of the supercooled liquid and the extent of structural relaxations in the glass. This connection has been recently discussed for GeAsSe alloys in Ref. [65] on the basis of the Adam-Gibbs model of the fragility which predicts that a larger fragility of the supercooled liquid would correlate with a larger propensity for structural relaxations as the temperature drops below T_g. Our NN simulations on GeTe demonstrate at the atomistic level that indeed the same structural features responsible for the high mobility close to T_g, typical of fragile liquids, are also responsible for the structural relaxations in the glass that generate the drift in the electrical resistance.

These results suggest that, in the search for better performing materials for PCM, a compromise must be reached between the requests of minimization of the resistance drift and of maximization of the crystallization speed in the set operation. These two properties in fact originate from the same structural features that control both the mobility in the supercooled liquid (where crystallization takes place) and the structural relaxations in the glass responsible for the resistance drift.

[1] M. Wuttig and N. Yamada, Nat. Mater. **6**, 824 (2007).

[2] A. Pirovano, A. L. Lacaita, F. Pellizzer, S. A. Kostylev, A. Benvenuti, and R. Bez, IEEE Trans. Electron Devices **51**, 714 (2004); D. Ielmini, A. L. Lacaita, and D. Mantegazza, *ibid.* **54**, 308 (2007).

[3] A. L. Lacaita and D. J. Wouters, Phys. Status Solidi A **205**, 2281 (2008).

[4] D. Lencer, M. Salinga, and M. Wuttig, Adv. Mater. **23**, 2030 (2011); S. Raoux, W. Welnic, and D. Ielmini, Chem. Rev. **110**, 240 (2010).

[5] G. E. Ghezzi, J. Y. Raty, S. Maitrejean, A. Roule, E. Elkaim, and F. Hippert, Appl. Phys. Lett. **99**, 151906 (2011).

[6] Y. T. Kim, E. T. Kim, C. S. Kim, and J. Y. Lee, Phys. Status Solidi RRL **5**, 98 (2011).

[7] H. Y. Cheng, S. Raoux, and J. L. Jordan-Sweet, Appl. Phys. Lett. **98**, 121911 (2011).

[8] A. Sebastian, N. Papandreou, A. Pantazi, H. Pozidis, and E. Eleftheriou, J. Appl. Phys. **110**, 084505 (2011).

[9] J. Luckas, A. Piarristeguy, G. Bruns, P. Jost, S. Grothe, R. M. Schmidt, C. Longeaud, and M. Wuttig, J. Appl. Phys. **113**, 023704 (2013).

[10] I. V. Karpov, M. Mitra, D. Kau, G. Spadini, Y. A. Kryukov, and V. G. Karpov, J. Appl. Phys. **102**, 124503 (2007).

[11] J. Im, E. Cho, D. Kim, H. Horii, J. Ihm, and S. Han, Curr. Appl. Phys. **11**, e82 (2011).

[12] M. Mitra, Y. Jung, D. S. Gianola, and R. Agarwal, Appl. Phys. Lett. **96**, 222111 (2010).

[13] M. Rizzi, A. Spessot, P. Fantini, and D. Ielmini, Appl. Phys. Lett. **99**, 223513 (2011).

[14] M. Boniardi and D. Ielmini, Appl. Phys. Lett. **98**, 243506 (2011).

[15] P. Fantini, S. Brazzelli, E. Cazzini, and A. Mani, Appl. Phys. Lett. **100**, 013505 (2012).

[16] C. Longeaud, J. Luckas, D. Krebs, R. Carius, J. Klomfass, and M. Wuttig, J. Appl. Phys. **112**, 113714 (2012).

[17] D. Ielmini and Y. Zhang, Appl. Phys. Lett. **90**, 192102 (2007).

[18] D. Krebs, T. Bachmann, P. Jonnalagadda, L. Dellman, and S. Raoux, New J. Phys. **16**, 043015 (2014).

[19] K. V. Mitrofanov, A. V. Kolobov, P. Fons, X. Wang, J. Tominaga, Y. Tamenori, T. Uruga, N. Ciocchini, and D. Ielmini, J. Appl. Phys. **115**, 173501 (2014).

[20] S. Caravati, M. Bernasconi, T. D. Kühne, M. Krack, and M. Parrinello, Appl. Phys. Lett. **91**, 171906 (2007).

[21] J. Akola and R. O. Jones, Phys. Rev. B **76**, 235201 (2007).

[22] J. Hegedüs and S. R. Elliott, Nat. Mater. **7**, 399 (2008).

[23] R. Mazzarello, S. Caravati, S. Angioletti-Uberti, M. Bernasconi, and M. Parrinello, Phys. Rev. Lett. **104**, 085503 (2010).

[24] See Supplemental Material at http://link.aps.org/supplemental/10.1103/PhysRevB.92.054201 for additional data on electronic and structural properties of the a-GeTe models.

[25] M. Krbal, A. V. Kolobov, P. Fons, K. V. Mitrofanov, Y. Tamenori, J. Hegedus, S. R. Elliott, and J. Tominaga, Appl. Phys. Lett. **102**, 111904 (2013).

[26] G. C. Sosso, G. Miceli, S. Caravati, J. Behler, and M. Bernasconi, Phys. Rev. B **85**, 174103 (2012).

[27] J. Behler and M. Parrinello, Phys. Rev. Lett. **98**, 146401 (2007); J. Behler, J. Chem. Phys. **134**, 074106 (2011).

[28] A. Laio and M. Parrinello, Proc. Natl. Acad. Sci. USA **99**, 12562 (2002).

[29] A. Laio and F. L. Gervasio, Rep. Prog. Phys. **71**, 126601 (2008).

[30] A. Barducci, M. Bonomi, and M. Parrinello, Wires Comput. Mater. Sci. **1**, 826 (2011).

[31] J. P. Perdew, K. Burke, and M. Ernzerhof, Phys. Rev. Lett. **77**, 3865 (1996).

[32] G. C. Sosso, J. Behler, and M. Bernasconi, Phys. Status Solidi B **249**, 1880 (2012).

[33] G. C. Sosso, D. Donadio, S. Caravati, J. Behler, and M. Bernasconi, Phys. Rev. B **86**, 104301 (2012).

[34] G. C. Sosso, G. Miceli, S. Caravati, J. Behler, and M. Bernasconi, J. Phys. Chem. Lett. **4**, 4241 (2013).

[35] G. C. Sosso, J. Colombo, E. Del Gado, J. Behler, and M. Bernasconi, J. Phys. Chem. B **118**, 13621 (2014).

[36] J. Behler, *RuNNer–A Neural Network Code for High-Dimensional Potential-Energy Surfaces*, Lehrstuhl für Theoretische Chemie, Ruhr-Universität Bochum, Bochum, Germany, http://www.theochem.ruhr-uni-bochum.de/~joerg.behler/runner.htm.

[37] W. Smith and T. R. Forester, J. Mol. Graph. **14**, 136 (1996).

[38] G. Bussi, D. Donadio, and M. Parrinello, J. Chem. Phys. **126**, 014101 (2007).

[39] J. Im, E. Cho, D. Kim, H. Horii, J. Ihm, and S. Han, Phys. Rev. B **81**, 245211 (2010).

[40] J. VandeVondele *et al.*, Comput. Phys. Commun. **167**, 103 (2005); www.cp2k.org.

[41] S. Goedecker, M. Teter, and J. Hutter, Phys. Rev. B **54**, 1703 (1996); M. Krack, Theor. Chem. Acc. **114**, 145 (2005).

[42] Y. Waseda, *The Structure of Non-Crystalline Materials* (McGraw-Hill, New York, 1980).

[43] L. Giacomazzi, P. Umari, and A. Pasquarello, Phys. Rev. B **74**, 155208 (2006).

[44] E. Engel and S. H. Vosko, Phys. Rev. B **47**, 13164 (1993).

[45] S. Caravati, M. Bernasconi, T. D. Kühne, M. Krack, and M. Parrinello, J. Phys.: Condens. Matter **21**, 255501 (2009); **21**, 499803 (2009); **22**, 399801 (2010).

[46] W. Welnic, S. Botti, M. Wuttig, and L. Reining, C. R. Phys. **10**, 514 (2009).

[47] S. Caravati, M. Bernasconi, and M. Parrinello, J. Phys.: Condens. Matter **22**, 315801 (2010).

[48] S. Caravati and M. Bernasconi, Phys. Status Solidi B **252**, 260 (2015).

[49] M. Xu, Y. Q. Cheng, H. W. Sheng, and E. Ma, Phys. Rev. Lett. **103**, 195502 (2009).

[50] S. Caravati, M. Bernasconi, and M. Parrinello, Phys. Rev. B **81**, 014201 (2010).

[51] J. Goldak, C. S. Barrett, D. Innes, and W. Youdelis, J. Chem. Phys. **44**, 3323 (1966).

[52] L. E. Shelimova and S. K. Plachkova, Phys. Status Solidi A **104**, 679 (1987).

[53] J. R. Errington and P. G. Debenedetti, Nature (London) **409**, 318 (2001).

[54] G. C. Sosso, S. Caravati, and R. Mazzarello, and M. Bernasconi, Phys. Rev. B **83**, 134201 (2011).

[55] E. Spreafico, S. Caravati, and M. Bernasconi, Phys. Rev. B **83**, 144205 (2011).

[56] J. H. Los, T. D. Kühne, S. Gabardi, and M. Bernasconi, Phys. Rev. B **88**, 174203 (2013).

[57] P. J. Steinhardt, D. R. Nelson, and M. Ronchetti, Phys. Rev. B **28**, 784 (1983).

[58] J. S. van Duijneveldt and D. Frenkel, J. Chem. Phys. **96**, 4655 (1992).

[59] V. L. Deringer, W. Zhang, M. Lumeij, S. Maintz, M. Wuttig, R. Mazzarello, and R. Dronskowski, Angew. Chem. Int. Ed. **53**, 10817 (2014).

[60] F. Zipoli and A. Curioni, Proceedings of E\PCOS, Berlin, 2013, http://www.epcos.org/library/library2013.htm.

[61] P. G. Debenedetti and F. H. Stillinger, Nature (London) **410**, 259 (2010).

[62] C. A. Angell, Science **267**, 1924 (1995).

[63] J. Orava, A. L. Greer, B. Gholipour, D. W. Hewak, and C. E. Smith, Nat. Mater. **11**, 279 (2012).

[64] A. L. Lacaita and A. Redaelli, Microelectron. Eng. **109**, 351 (2013).

[65] T. Wang, O. Gulbiten, R. Wang, Z. Yang, A. Smith, B. Luther-Davies, and P. Lucas, J. Phys. Chem. B **118**, 1436 (2014).